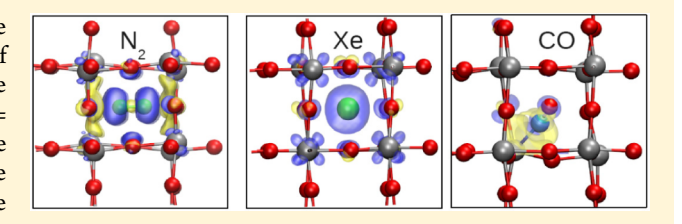


# Tungsten Oxide Clathrates for Water Oxidation: A First Principles Study

Yuan Ping,\*,† Yan Li,‡ Francois Gygi,§ and Giulia Galli†,||

Supporting Information

ABSTRACT: Tungsten oxide (WO<sub>3</sub>) is a good photoanode material for oxidizing water, but it is not an efficient absorber of sunlight because of its large band gap (2.6 eV). Recently, stable clathrates of WO<sub>3</sub> with interstitial N<sub>2</sub> molecules ( $xN_2 \cdot WO_3$ , x =0.034-0.039) were synthesized, with a band gap of 1.8 eV. We studied the structural and electronic properties of these clathrates using ab initio calculations, and we analyzed the physical origin of the gap reduction reported experimentally. We



found that both structural changes caused by the insertion of N<sub>2</sub>, and a small charge overlap between N<sub>2</sub> and WO<sub>3</sub>, are responsible for the gap decrease. We compared the effect of N<sub>2</sub> intercalation to that of other closed shell species, in particular CO and rare gas atoms. Our calculations predicted that CO insertion lowers the band gap by about the same amount as N<sub>2</sub> but it leads to a change of both the oxide valence and conduction band positions, while the presence of N<sub>2</sub> only affects the conduction band minimum. We also predicted that, in the case of Xe, a strong hybridization between Xe 5p and O 2p states modifies the valence band edge of WO<sub>3</sub>, leading to a reduction of the band gap by approximately 1 eV.

KEYWORDS: tungsten oxide clathrates, band gap, water oxidation

# ■ INTRODUCTION

Tungsten oxide (WO<sub>3</sub>) has been extensively studied for its potential use as an anode material in photovoltaic and photoelectrochemical cells; 1-8 however, its band gap far exceeds 1.23 eV, the minimum energy per electron required for water oxidation at standard conditions, and a number of investigations have been focused on lowering the band gap of this material either by doping or structural modifications. 5 Tungsten oxide has the perovskite structure (ABO<sub>3</sub>) where the central "A" site is not occupied. The "A" position may be filled by dopants (e.g., H, Li, or Na) leading to intricate structural changes, e.g., to cubic structures for  $H_{0.5}WO_3$ ,  $Li_xWO_3$  (0.1 < x< 0.4) and Na<sub>x</sub>WO<sub>3</sub> (0.3 < x < 1). Doping WO<sub>3</sub> with alkali metals changes both the crystal structure and the electronic and optical properties. For example, the color of Na<sub>x</sub>WO<sub>3</sub> may be tuned from greenish to yellow as x is increased from 0 to 1, 15 and the WO<sub>3</sub> unit cell volume expands by 7.3% at x = 1.16,17The incorporation of alkali ions results in the formation of an sband high above the Fermi level and to the formation of a metallic conductor. 16,18

Recently much effort was devoted to N-doping of oxides which are promising photoanodes, including WO<sub>3</sub> and TiO<sub>2</sub>. Nitrogen substitution of O was shown to extend the light absorption onset from 380 nm to visible light (above 500 nm) in TiO<sub>2</sub>, thus offering possible photocatalytic activity under visible light irradiation. <sup>19–21</sup> However, N-doping usually yielded a lower photocurrent under a full spectrum and a lower quantum yield in the UV region than pure TiO2. The reason for the photocurrent decrease is under debate: it was proposed<sup>22,20,23</sup> that substitutional N leads to isolated midgap states which are highly localized and act as recombination centers. An alternative explanation is based on the hybridization of N and O 2p orbitals, which is expected to shift the valence band edge of the oxide to more negative potentials, thus providing a less favorable alignment with the water redox potential.<sup>24</sup> Atomic N doping of WO<sub>3</sub> was studied in several recent papers. 9,10 It was found that N substitution leads to a significant decrease of the band gap of WO<sub>3</sub><sup>10</sup> for N concentrations larger than 2%. Unfortunately, this high concentration of N gives rise to charged defects 9,25,26 and increases carrier recombination rates, thus leading to a poor photocurrent density.

Recently it was shown that doping (or intercalation) of N<sub>2</sub> into WO<sub>3</sub> leads to the formation of stable clathrates<sup>27</sup> without adding charged defects to the system, thus avoiding the formation of undesired carrier recombination centers. By intercalating N2 into WO3, the band gap was reduced by ~0.8 eV, compared to that of room temperature (RT)

October 4, 2012 Received: Revised: October 16, 2012 Published: October 17, 2012

<sup>&</sup>lt;sup>†</sup>Department of Chemistry, University of California, Davis, California 95616, United States

<sup>&</sup>lt;sup>‡</sup>Computational Science Center, Brookhaven National Laboratory, Upton, New York 11973, United States

<sup>§</sup>Department of Computer Science, University of California, Davis, California 95616, United States

Department of Physics, University of California, Davis, California 95616, United States

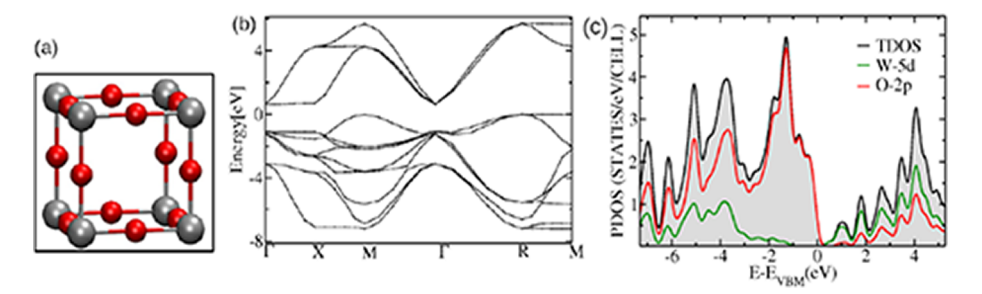


Figure 1. Band structure (b) and projected density of states (PDOS) and total density of states (TDOS) (c) of simple cubic WO<sub>3</sub> as obtained with DFT/LDA calculations. In panel c, the zero of energy has been chosen at the VBM ( $E_{VBM}$ ). The crystal structure is shown in part a.

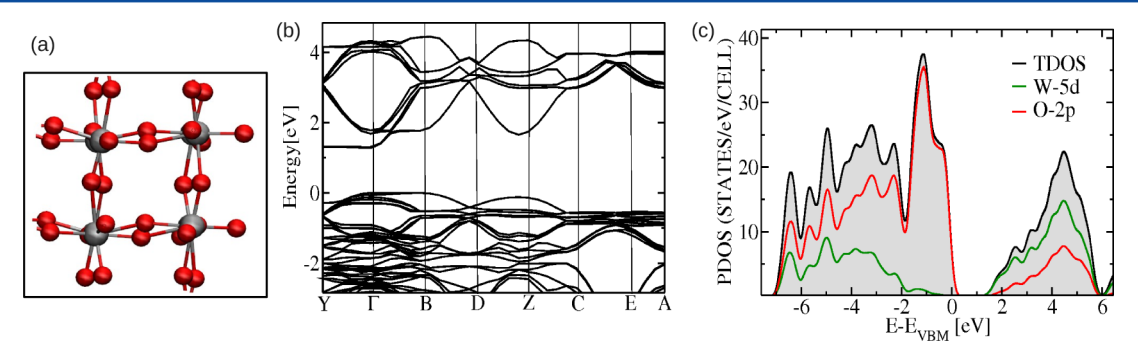


Figure 2. Band structure (b) and projected density of states (PDOS) and total density of states (TDOS) (c) of monoclinic WO<sub>3</sub> as obtained with DFT/LDA calculations. In panel c, the zero of energy has been chosen at the VBM ( $E_{VBM}$ ). The crystal structure is shown in part a.

monoclinic WO<sub>3</sub>. This observation suggests that the formation of clathrates is a promising route to improve the absorption efficiency of WO<sub>3</sub>, and it is interesting to search for other small molecules or atoms that may induce a desired gap decrease upon intercalation in WO<sub>3</sub>. We note that N<sub>2</sub> intercalation was reported in several (Ba)–Ti–O systems with the perovskite structure, where the presence of dinitrogen was characterized using X-ray photoelectron (XPS) and Raman spectroscopy. A slight increase in the unit cell volume upon nitrogen molecules intercalation was observed in several cases, and all reactions were found to be endothermic.

In this study, we present first principles calculations of tungsten oxide compounds intercalated with molecular nitrogen, CO, and rare gas atoms, and we show that both structural changes, and electronic interactions between the matrix and the guest species, lead to a lowering of the band gap. Structural changes are the major effect. Our results provide a detailed interpretation of experiments in the case of N<sub>2</sub>, and predictions on other stable clathrates with promising properties for water oxidation.

# COMPUTATIONAL METHODS

We performed first principles calculations within the framework of density functional theory (DFT) using the Quantum Espresso package  $^{30}$  and the Qbox code,  $^{31}$  and different levels of theory [the local density approximation (LDA), the generalized gradient approximation (GGA) using the PBE $^{32}$  functional, the hybrid functional PBE $^{33}$  nonlocal van der Waals functional vdW-DF2,  $^{34-38}$  and the modified self-consistent field method proposed in ref 39]. Our LDA results for the structural properties of cubic and monoclinic WO3 are in agreement with previous calculations  $^{9,16,40-42}$  (see Tables S1 and S2 in the Supporting Information). The LDA predicted equilibrium volume deviates from experiment by less than 1%, whereas PBE and the functional vdW-DF2  $^{34-38}$  overestimate the equilibrium volume by  $\sim$ 5%. In the calculations of the intercalated systems, we primarily used the LDA, as we focus on discussing trends

in computed properties rather than on absolute values of computed gaps and total energies.

Consistent with previous results, 9,16,40-42 we found that LDA and PBE calculations underestimate the band gap of monoclinic WO<sub>3</sub> by about 50%, when both the lattice constants and the internal geometry are optimized, while vdW-DF2 yields a larger gap than both LDA and PBE. We note that DFT geometry optimizations yielded reduced structural distortions in monoclinic WO3, relative to those reported experimentally; in turn this leads to, e.g., at the LDA (vdW-DF2) level a moderate decrease of the band gap from 1.87(2.04) eV at the experimental geometry to 1.46(2.01) eV when computed at the experimental lattice parameters  $(V_{\text{exp}})$  but allowing for internal structural relaxations, and finally to 1.30(1.80) eV when evaluated at the fully optimized DFT geometry. To obtain a quantitative estimate of the band gap, we used the modified self-consistent field (SCF) approach recently proposed for solids in ref 39 (hereafter referred to as modified  $\Delta SCF$  approach): we found that the band gap of monoclinic WO<sub>3</sub> is 2.90 eV at the experimental geometry, and 2.39 eV at the LDA relaxed geometry; these values are much closer to the measured room temperature band gap of 2.60 eV than those obtained within LDA, PBE, or vdW-DF2. We also carried out calculations at the PBE0 level of theory, using the LDA optimized geometry. The computed band gap is 3.28 eV, higher than in experiments, and consistent with the value of 3.67 eV reported in ref 43.44

All of our calculations for clathrates ( $N_2$ , CO, and rare gases in WO<sub>3</sub>) were carried out for the monoclinic geometry of the oxide. In the case of  $N_2$  we also compared our results with those obtained by intercalating  $N_2$  into cubic WO<sub>3</sub>.

#### ■ RESULTS AND DISCUSSION

We first report our results for the structural and electronic properties of pure  $WO_3$ , and we then discuss the properties of  $N_2$ , CO, and rare gas intercalated  $WO_3$ .

**Pure WO<sub>3</sub>.** The band gap of WO<sub>3</sub> is known to be extremely sensitive to the detailed crystallographic arrangement of the octahedra. Therefore, before investigating WO<sub>3</sub> clathrates we analyzed in detail how lattice distortions of pure WO<sub>3</sub> influence

the band structure and band gap of the material; we focused on the cubic and monoclinic phases.

Monoclinic WO<sub>3</sub> is a distorted structure compared to the simple cubic solid: W atoms are located off the octahedra centers and the tilt angle between octahedra, denoted as  $\theta_{t}$ , deviates from 180° by 15-25°(see Figures 1a and 2a). At elevated temperatures, monoclinic WO3 transforms to high symmetry structures: to an orthorhombic solid at 330-740°, and subsequently to a tetragonal phase at 740°. These transformations are accompanied by a volume expansion of  $2-3\%^{46,47}$  and by a band gap reduction from 2.6 eV (monoclinic WO<sub>3</sub>) to 1.8 eV (tetragonal WO<sub>3</sub>). To identify the main geometrical factors responsible for the gap reduction upon volume expansion, we compared the variation of the gap  $(E_{\sigma})$  with volume (V) in monoclinic and cubic WO<sub>3</sub>. The slope  $dE_g/dV$  found experimentally is 0.2–0.3 eV/Å<sup>3</sup>/WO<sub>3</sub>,<sup>48,49</sup> higher than our computed value using the LDA functional, 0.09 eV/Å<sup>3</sup>/WO<sub>3</sub>, which is similar to those of other DFT calculations  $^{40,43}$  (d $E_{\rm g}/{\rm d}V=0.1~{\rm eV/\AA^3}$  in the LDA calculation of ref 40 and 0.085 eV/Å<sup>3</sup> in the B3LYP calculation of ref 43, see Figure S1 in the Supporting Information). In contrast, the computed slope of simple cubic WO<sub>3</sub> is much smaller (0.02 eV/Å<sup>3</sup>/WO<sub>3</sub>). These results indicate that the variation of tilt angles, i.e., the relative rotation angles of the almost rigid octahedra, is mainly responsible for the band gap reduction during the lattice expansion of monoclinic WO3. Indeed, the linear coefficient between the band gap and the volume is rather small in the simple cubic phase, where the tilt angle is always 180°.

The effect of tilt angles on the band gap was further investigated by using different functionals. Figure 3 shows the

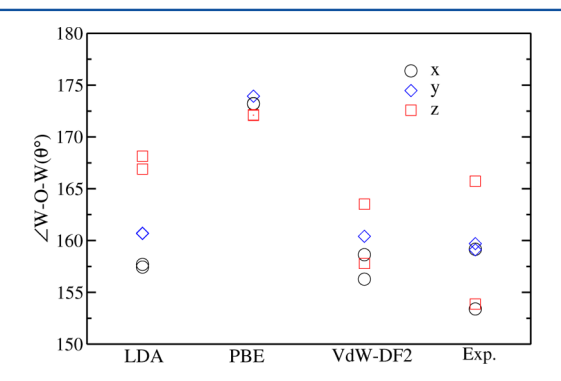


**Figure 3.** W–O tilt angles of monoclinic WO<sub>3</sub> obtained with different functionals, LDA, PBE, vdW-DF2, and at experimental geometry (Exp). In each panel "x, y, z" denote the tilt angles along the x, y, z directions, respectively. As  $\beta$  is close to 90 (within 1), the x, y, z directions are roughly parallel to the a, b, c lattice vectors. Hence W–O chains are almost parallel to each of the three Cartesian axes.

W–O tilt angles of monoclinic WO $_3$  optimized with LDA, PBE, and vdW-DF2 functionals, as well as at the experimental geometry. Both PBE and LDA overestimate the octahedra tilt angles  $\angle$ W–O–W; instead, vdW-DF2 yields a range of tilt angles similar to the experimental ones, leading to a computed band gap in better agreement with experiment than LDA and PBE (see Table S2 in the Supporting Information).

The LDA computed band gap of the simple cubic structure is 0.53 eV, and it is indirect from R (0.5,0.5,0.5) to  $\Gamma$ . The valence band maximum (VBM) is mainly composed of O nonbonding 2p states ( $p_x$ ,  $p_y$ ,  $p_z$  are degenerate), whereas the conduction band minimum (CBM) is composed of W 5d  $t_{2g}$  states ( $d_{xy}$ ,  $d_{yz}$ )

 $d_{xz}$  are degenerate) and O 2p states. The metal d orbitals are split by the octahedral field of oxygen ligands, with  $t_{2g}$  levels at lower energy than  $e_g$  levels. There is a considerable amount of hybridization between O 2p and W 5d bands, which can be clearly seen from the projected density of states (PDOS) reported in Figure 1c. The mixing of W 5d and O 2p yields bonding states belonging to the valence band, and antibonding states contributing to the conduction band.

The VBM of RT monoclinic WO<sub>3</sub> is located at B (0.5, 0, 0), as shown in the band structure computed within the LDA in Figure 2b. From  $\Gamma$  to B, the band is nearly dispersionless, implying a very high effective hole mass perpendicular to the W–O–W chain in the x direction. The CBM is located at the  $\Gamma$  point, and the computed band gap is 1.3 eV (at the LDA level). Note that the PDOS of monoclinic WO<sub>3</sub>, shown in Figure 2c, is similar to that of simple cubic WO<sub>3</sub>: in both cases the onset of W 5d and O 2p hybridization in the valence band occurs about 1 eV below the VBM, the pure oxygen states at the VBM arise from unshared oxygen electrons occupying orbitals oriented perpendicular to the W–O bonds, and the CBM is composed of hybridized W 5d and O 2p states.

Figure 4 compares the band structure of monoclinic WO<sub>3</sub> as obtained using the PBE (black) and the vdW-DF2 (red)

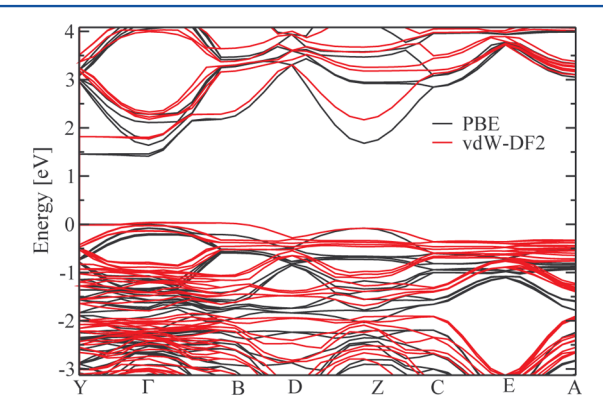


Figure 4. Band structure of pure monoclinic  $WO_3$  obtained by DFT calculations using the PBE (black) and vdW-DF2 (red) functionals.

functionals (both calculations were carried out with the same PBE pseudopotential). The bottom of the CBM is shifted upward with vdW-DF2, compared to PBE, but the VBM position is very similar. This is consistent with the octahedra tilt angle found in the two cases, which is smaller with vdW-DF2 than with PBE, thus leading to a decrease of the overlap between the W 5d and O 2p orbitals at the CBM, and of the 5d–2p hybridization. On the other hand, the VBM is composed by O nonbonding states which are less sensitive to the crystal geometry.

N<sub>2</sub> Intercalated WO<sub>3</sub>. Structural Properties. We now turn to the discussion of the structural and electronic modifications occurring in WO<sub>3</sub> upon N<sub>2</sub> insertion. We showed that the top of the valence band of WO<sub>3</sub> is mostly composed of O nonbonding 2p orbitals, which are hardly affected by the coordination environment; nevertheless, an element less electronegative than O, e.g., N, may help raise the VB edge. However, doping WO<sub>3</sub> by N substitution of O is likely to form electron—hole recombination centers which then have a negative effect on the photocatalytic activity of the material, as discussed in the Introduction. A different way of lowering the band gap was recently proposed, by doping WO<sub>3</sub> with

molecular nitrogen. Stable clathrate compounds with composition  $xN_2 \cdot WO_3$ , x = 0.034-0.039, were prepared by trapping  $N_2$  in  $WO_3$ . The incorporation of  $N_2$  significantly reduced the band gap of the monoclinic phase  $WO_3$ , up to 0.8 eV, the exact value depending on the annealing temperature.

Assuming the absence of other defects in the  $N_2$ -intercalated WO<sub>3</sub>, our calculations showed that the band gap reduction may be attributed to two factors. One is the orbital coupling between  $N_2$  and WO<sub>3</sub>, accompanied by a small charge overlap. In addition,  $N_2$  exerts an effective stress on the WO<sub>3</sub> lattice, causing a structural change. We first discuss the structural changes occurring in WO<sub>3</sub> upon  $N_2$  insertion, which are mostly responsible for the gap decrease, and then we examine the modification of the electronic structure of the host oxide in the presence of  $N_2$ .

Figure 5 shows the bond lengths and tilt angles of the octahedra of pure monoclinic WO<sub>3</sub> and N<sub>2</sub>-intercalated WO<sub>3</sub>

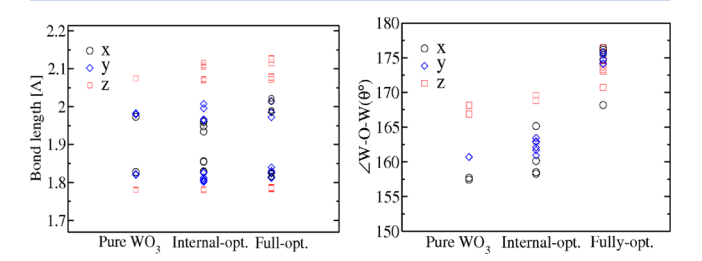


Figure 5. Bond length (left panel) and tilt angle (right panel) of pure monoclinic  $WO_3$  and  $N_2$ -intercalated  $WO_3$  with concentration  $1N_2$ :8 $WO_3$  optimized using the LDA functional. In each panel, the first column (Pure- $WO_3$ ) corresponds to the optimized geometry of pure monoclinic  $WO_3$ , the second column (Internal-opt.) corresponds to the geometry of  $N_2$ -intercalated  $WO_3$  where only the internal coordinates were optimized while keeping the same cell parameters as those of pure monoclinic  $WO_3$ , and the third column (Fully opt.) corresponds to the geometry of  $N_2$ -intercalated  $WO_3$  where both the internal coordinates and the cell parameters were optimized. In each panel "x, y, z" denote the bond lengths or tilt angles along the x, y, z directions, respectively. As β is close to 90 (within 1), the x, y, z directions are roughly parallel to the a, b, c lattice vectors. Hence W-O chains are almost parallel to each of the three Cartesian axes.

(1N<sub>2</sub>:8WO<sub>3</sub>) as a function of the structural parameters varied in our geometry optimizations (internal coordinates and cell parameters) at the LDA level. The left panel shows that N<sub>2</sub> doping causes slightly larger bond length splitting (BLS) (on average by 0.017 Å) than those found in pure WO<sub>3</sub> in all the three directions, for both internally and fully optimized N2doped WO<sub>3</sub>. Figure 5 also shows that the bond angle  $\angle$ W-O-W exhibits small variations when only internal coordinates are optimized in N2-intercalated WO3; in contrast, upon full optimization including the cell parameters, the volume of N2intercalated WO<sub>3</sub> increases by 5% and the ∠W-O-W increases from 155-165° to 170-175°. The structural changes obtained by fully optimizing N2-intercalated WO3 are similar to those observed in the lattice expansion of monoclinic WO<sub>3</sub> (see Figure S2 in the Supporting Information) where ∠W-O-W increased by 10–15° with 5% volume expansion.

To investigate the stability of  $N_2$  in the oxide, we computed the energy change for incorporation of  $N_2$  into  $WO_3$  as  $\Delta E$  in Table 2 shows. For all  $N_2$  intercalated configurations studied here, we found that the energy change is about +1.6 eV; the positive value indicates that the intercalation process is endothermic. This result is consistent with those of  $N_2$ -

containing perovskite compounds (La–Ba–Ti systems) reported in ref 29: calorimetric experiments have shown that incorporation of  $N_2$  in these compounds is an endothermic reaction. However,  $N_2$ -containing perovskite compounds (La–Ba–Ti systems) are stable under ambient conditions, indicating that  $N_2$  molecules are kinetically trapped into the oxide lattices. This is again similar to what was found here in the case of  $N_2$  in  $WO_3$ . By using nudge elastic band calculations,  $^{51}$  we found that the kinetic barrier for  $N_2$  to diffuse from a hollow center of the  $WO_3$  crystal to a neighboring hollow center is 2.6 eV, indicating that  $xN_2$ ·WO $_3$  is kinetically stable (thermal energy RT=0.067 eV at 750 °C) although not thermodynamically stable.

Experimentally, <sup>27</sup> Raman and NMR spectroscopies were used to characterize  $N_2$  into  $WO_3$  and to better understand the structural properties of the clathrate. In the measured Raman spectra of  $xN_2 \cdot WO_3$ , x = 0.034-0.039, the maximum corresponding to the N–N stretching frequency was found to split into two peaks around the gas phase value: a sharp one red-shifted by 4 cm<sup>-1</sup> and a broad one blue-shifted by 8 cm<sup>-1</sup>. We carried out a series of calculations at the LDA level to interpret the observed vibrational signatures. We first computed the frequency of gas phase  $N_2$  and obtained a value of 2383 cm<sup>-1</sup>, which is 25 cm<sup>-1</sup> higher than the experimental one (2330 cm<sup>-1</sup>) after anharmonic corrections,  $\nu_{\rm exp}^{\rm corrected} = 2358.6$  cm<sup>-1</sup>.

As the errors caused by the use of approximate exchange-correlation approximations and the neglect of anharmonic effects are most likely systematic,  $^{52}$  we expect the use of such approximations to yield the correct trend of the frequency shift within different environments, e.g., in the gas phase or within WO<sub>3</sub>. When computing the N<sub>2</sub> frequency in the oxide, we carried out two sets of calculations: one where the WO<sub>3</sub> lattice was kept frozen and one where all atoms were allowed to move. The results of the two sets of calculations for the vibrational frequencies of N<sub>2</sub> differed by at most 1 cm<sup>-1</sup>, confirming that the vibrational properties of the guest molecule are not affected by those of the host oxide.

Tables 1 and 2 list the structural, vibrational, and bonding properties of interstitial  $N_2$  in simple cubic and monoclinic

Table 1. Structural, Bonding, and Vibrational Properties of an Interstitial N<sub>2</sub> Molecule in Simple Cubic WO<sub>3</sub>, Oriented along Different Directions, at the "A" Site of the "ABO<sub>3</sub>" Structure<sup>a</sup>

	$d_{\mathrm{N-N}}$ (Å)	$d_{\mathrm{N-W}}$ (Å)	$d_{\mathrm{N-O}}$ (Å)	$\Delta E \; (\mathrm{eV})$	$\nu  \left( \mathrm{cm}^{-1} \right)$
⟨100⟩	1.090	3.018	2.437	1.648	2397
$\langle 111 \rangle$	1.090	3.044	2.381	1.496	2408
gas phase	1.094				2383

<sup>a</sup>ΔE is the change of total energy obtained after the insertion of N<sub>2</sub> [ $\Delta E = E(8WO_3 \cdot N_2) - E(8WO_3) - E(N_2)$ ], and positive values indicate that such process is endothermic. "d" indicates distances and " $\nu$ " frequencies.

 $WO_3$ , respectively. We note that the frequency  $(\nu)$  and bond distance  $(d_{N-N})$  of a  $N_2$  molecule placed in a monoclinic unit cell of  $WO_3$  in the absence of the oxide (configuration e in Table 2) are almost identical to those of the gas phase, indicating that the interaction between  $N_2$  molecules in different unit cells is negligible.

In the case of  $N_2$ -intercalated simple cubic  $WO_3$ , we found that  $\nu$  always increases regardless of the molecular orientation, and the bond length is decreased by about 0.4–0.5%. Instead, the frequency of  $N_2$  in intercalated monoclinic  $WO_3$  exhibits a

Table 2. Structural, Bonding and Vibrational Properties of an Interstitial N<sub>2</sub> Molecule in Monoclinic WO<sub>3</sub>, Oriented along Different Directions, at the "A" Site in the "ABO<sub>3</sub>" Structure<sup>a</sup>

configuration	orientation	$ \overset{d_{\rm N-N}}{(\rm \AA)} $	$ \overset{d_{\rm N-W}}{(\rm \AA)} $	$\overset{d_{\rm N-O}}{(\rm \AA)}$	$\frac{\Delta E}{(\mathrm{eV})}$	$(\text{cm}^{-1})$
a	$\langle 100 \rangle$	1.091	3.037	2.464	1.669	2391
Ь	$\langle 010 \rangle$	1.090	2.982	2.451	1.722	2391
c	⟨001⟩	1.091	3.045	2.457	1.631	2389
d	$\langle 111 \rangle$	1.092	2.251	2.326	1.865	2373
e		1.094			0	2382
gas phase		1.094				2383

"Results are given for fully relaxed geometries. Configuration e denotes that of a  $N_2$  molecule placed in a monoclinic cell in the absence of the WO $_3$  lattice.  $^{27}$  d,  $\Delta E$ , and  $\nu$  have the same meaning as in Table 1.

strong orientation dependence (see Table 2): Configurations a, b, c have higher frequencies whereas configuration d has a lower frequency than gas phase  $N_2$ . The total energy difference between configurations a, b, and c is rather small (within 0.1 eV), which implies that all these geometrical arrangements may exist with similar probability at room temperature, thus explaining the broadening of the blue-shifted peak found in experiments.<sup>27</sup> In Tables 1 and 2, we also list the shortest distances between an N atom and either W or O atoms for both simple cubic and monoclinic WO<sub>3</sub>. These distances (e.g.,  $d_{\rm N-O}$  2.4–2.5 Å) are similar to those found, e.g., for  $N_2$  containing  $Ba_2Ta_2O_7N_{0.62}$  compounds.<sup>28,53</sup>

The shortening of the  $N_2$  bond length in configurations a-d is caused by the repulsive interaction between the  $WO_3$  lattice and the  $N_2$  molecule. The presence of  $N_2$  exerts a stress on the  $WO_3$  lattice, and the lattice tends to distort and expand in order to release this chemical pressure; the stress compresses the N-N bond leading to a decrease of the bond length.

Figure 6 shows the electron density difference  $(\Delta \rho)$  before and after  $N_2$  was inserted at interstitial sites in monoclinic

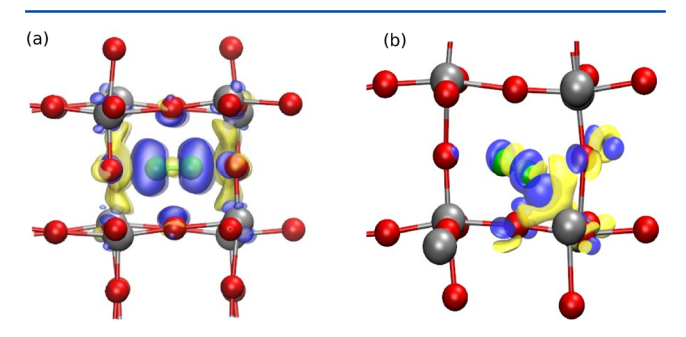


**Figure 6.** Electron density difference between pure monoclinic WO<sub>3</sub> and N<sub>2</sub> clathrates with N<sub>2</sub> oriented along the  $\langle 100 \rangle$  (a) and  $\langle 111 \rangle$  (b) directions. Yellow (blue) indicates electron depletion (accumulation). W and O atoms are represented by silver and red spheres, respectively; N atoms are represented by green spheres. The figures show isosurfaces of charge equal to 0.001  $e/a_0^3$ .

WO<sub>3</sub>:  $\Delta \rho = \rho(WO_3 + N_2) - \rho(WO_3) - \rho(N_2)$ . In both  $\langle 100 \rangle$  and  $\langle 111 \rangle$  directions, the electron density decreases in the region between two N atoms and increases in the region close to each N atom but away from the N–N bond. This indicates that the oxide lattice gains a small amount of electronic charge at the expenses of the nitrogen molecule. Thus,  $N_2$  is not completely inert inside the oxide lattices. In fact,  $N_2$  has been

shown to be weakly bonded to the oxide network  $^{29}$  in several  $N_2$  containing perovskite compounds. Charge density maps indicate that there is a larger charge overlap between  $N_2$  and  $WO_3$  in configuration d that weakens the N–N bonding; this may be responsible for a decrease in  $\nu$ , in contrast to other  $N_2$  orientations (see Table 2). These results explain the appearance of the red-shifted peak in the experimental Raman spectra,  $^{27}$  and the observed sharpness of this peak is consistent with the fact that  $\langle 111 \rangle$  is the only  $N_2$  orientation that corresponds to a red-shifted  $\nu$ .

Interestingly, a red-shifted vibrational frequency is not found in simple cubic  $WO_3$  (see Table 1), but it only occurs in monoclinic  $WO_3$ , likely because of the symmetry constraint in the cubic structure, preventing  $N_2$  to approach W or O as much as in the monoclinic phase. In the latter, the lattice distortion and lower symmetry allow  $N_2$  to get close (2.25 Å) to one of the W atoms (configuration d), leading to a significant charge overlap between  $N_2$  and W as shown in Figure 6b, and to a reduction in  $\nu$ .

Our results show that the observed changes in vibrational frequency of interstitial  $N_2$  may be explained by the presence of different orientations of the molecule within the host lattice. In some configurations, the repulsion between  $N_2$  and  $WO_3$  compresses the molecular bond and therefore leads to an increase of the molecular vibrational frequency; in other configurations the charge density redistribution between  $N_2$  and  $WO_3$  causes an electron density shifts from the bonding to the antibonding region of  $N_2$ , leading to a weakening of the N-N bonding and thus to a decrease of the vibrational frequency.

To further investigate whether the vibrational signatures observed experimentally are unique to intercalated  $N_2$ , we also examined the case of substitutional  $N_2$  and computed its vibrational properties. We considered the case where one O atom in the unit cell of the monoclinic WO<sub>3</sub> is replaced by a  $N_2$  molecule. The vibrational frequency of gas phase  $N_2$  decreases to 1713 cm<sup>-1</sup>, and the bond length increases to 1.197 Å (gas phase: 2383 cm<sup>-1</sup>, 1.094 Å). Therefore we concluded that the signal reported experimentally did not detect substitutional  $N_2$  molecules.

Electronic Structure. Having analyzed the structural and vibrational properties of the N2-WO3 clathrate, which are in agreement with experiments, 27 we now are in a position to investigate its electronic properties. We found that the LDA(vdW-DF2) band gap of fully optimized N<sub>2</sub>-intercalated WO<sub>3</sub> decreased by 0.2 eV (0.35 eV) compared to that of pure WO<sub>3</sub> at 1N<sub>2</sub>:8WO<sub>3</sub>, while the optimization of internal coordinates without volume variations led to a  $\approx 0.05$  (0.16) eV decrease. This suggests that the volume expansion and the increased ∠W−O−W angle are largely responsible for the band gap reduction found in the fully optimized N2-intercalated WO3. We obtained very similar band gap reductions using the PBE0 functional<sup>33</sup> and the modified  $\Delta SCF$  method<sup>39</sup> with the optimized LDA geometry. In particular the larger decrease in the gap obtained with the vdW-DF2 functional, which yields larger structural modifications upon insertion on N2 in the lattice than any other functional, emphasizes the importance of structural changes in determining the gap reduction.

The gap decrease of 0.2–0.35 eV predicted by theory is smaller than that found experimentally ( $\sim$ 0.8 eV). However we note that, by increasing the concentration of N<sub>2</sub> to 1:1, we obtained a band gap lowering of  $\sim$ 0.7 eV at the LDA level, consistent with the value 0.8 eV reported experimentally. These

results suggest that the  $N_2$  molecules may be clustered in experimental samples.

Figure 7 compares the band structure(LDA) of fully optimized monoclinic WO<sub>3</sub> intercalated by N<sub>2</sub> and pure

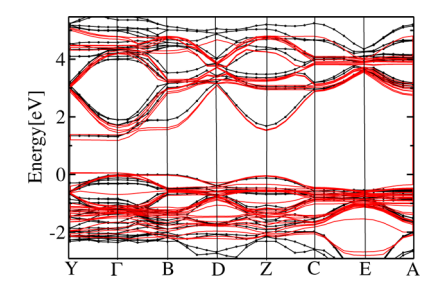


Figure 7. Band structure of  $N_2$ -intercalated monoclinic WO<sub>3</sub> (red) at  $1N_2$ :8WO<sub>3</sub> concentration as obtained by DFT-LDA calculations. For comparison, the band structure of pure monoclinic WO<sub>3</sub> obtained at the same level of theory is also shown (black).

WO<sub>3</sub>. By aligning the W 5s,5p core states of the two systems, we found that the CBM of the doped oxide is lowered but the VBM position is almost unchanged (there is just a small positive shift of 0.05 eV). As discussed previously, this could be due to a change in the tilt angle of two octahedra, that becomes ~180°, and to an increase in overlap between the W 5d and O 2p orbitals at the CBM, enhancing 5d–2p hybridization and shifting downward the CBM. On the other hand, the VBM is composed by O nonbonding states which are less sensitive to the crystal geometry. In both cases, the CBM is at the  $\Gamma$  point while the VBM is along Y(0,0.5,0)-B(0.5,0,0) where the band is nearly flat for the N<sub>2</sub> intercalated case. We found that the difference between direct and indirect band gap is less than 0.02 eV. This is the case also for the band structures computed by PBE and vdW-DF2 functionals.

Table 3 shows the equilibrium lattice parameters and band gap of  $N_2$  intercalated  $WO_3(8WO_3:1N_2)$  optimized at LDA,

Table 3. Equilibrium Lattice Parameters  $(a_0, b_0, c_0)$  of Monoclinic 8WO<sub>3</sub>:1N<sub>2</sub> and Its Band Gap  $(E_g)$  at the Fully Optimized Geometry<sup>a</sup>

	lattic	lattice parameters (Å)			
method	$a_0$	$b_0$	<i>c</i> <sub>0</sub>	$E_g$ (eV)	
LDA/HGH	7.57	7.57	7.72	1.13	
PBE/HGH	7.51	7.67	7.92	1.42	
vdW-DF2/HGH	7.57	7.75	8.09	1.45	

 $^{\prime\prime}$ α,  $^{\prime}$ β,  $^{\prime}$ γ are very close to 90, which are not listed here. LDA/HGH denotes results of calculations carried out within the LDA with HGH pseudopotentials,  $^{56}$  "PBE/HGH" denotes results of PBE calculations with HGH pseudopotentials, and "vdW-DF2/HGH" denotes results of vdW-DF2 calculations  $^{34-37}$  with HGH pseudopotentials.

PBE, vdW-DF2 functionals. Unlike pure monoclinic WO $_3$ , the band gaps obtained at the PBE and vdW-DF2 level of theory are very close (they differ by less than 0.1 eV). This is consistent with the fact that the tilt angles of  $8WO_3:1N_2$  obtained by PBE and vdW-DF2 all fall into the same range (between  $165^{\circ}-176^{\circ}$ ), and that the band structures obtained by PBE and vdW-DF2 are very similar (not shown), despite differences in the optimized lattice constants (see Table 3).

CO Intercalated WO<sub>3</sub>. Inspired by  $N_2$  intercalation, we studied other possible clathrates obtained by intercalating closed shell molecules and atoms, in particular CO and rare

gases. These materials have not yet been realized experimentally, and similar to the case of  $N_2$  we found that the formation of the clathrates is endothermic. Therefore the guest atoms or molecules will have to be kinetically trapped into the host oxide. Once trapping is achieved, large energy barriers (of the order of 2.9 eV for CO and 2.6 eV for  $N_2$  in our nudged elastic band<sup>57</sup> calculations) will prevent escape of the guest species. Again similar to  $N_2$  intercalation, the presence of CO and rare gas atoms does not induce any charged defects within the WO<sub>3</sub> crystal; thus, one avoids the formation of electronhole recombination centers found, e.g., in the case of N substitution and O vacancies.

Upon intercalation, CO binds to W along the  $\langle 111 \rangle$  direction with a C-W atomic distance of 2.1 Å (see Figure.8). This

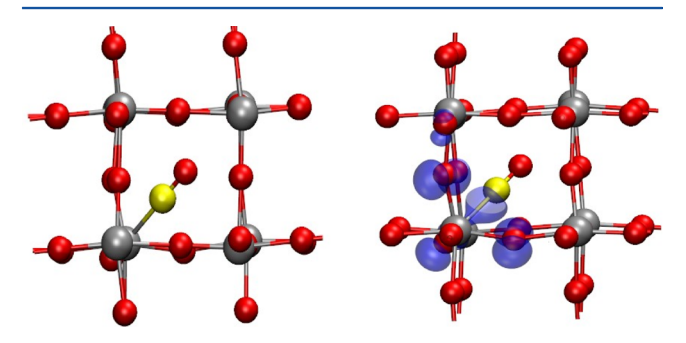


**Figure 8.** Geometry of CO intercalated in monoclinic  $WO_3$  (left panel) at  $1CO:8WO_3$  concentration and the squared modules of the wave function (right panel) at the VBM, at the high symmetric point A(-0.5,0.5,0).

bonded configuration is more favorable than the one with CO inside an octahedral cavity and not bonded to the lattice: for instance, the configuration with CO along the (100) direction has a total energy 0.5 eV higher than the configuration of Figure 8. Due to the Coulomb repulsion between carbon lone pair electrons and nearby O nonbonding p orbitals, the valence band edge of the oxide shifts upward in the presence of CO by  $\sim$ 0.15 eV, compared with that of pure monoclinic WO<sub>3</sub>. The wave function at the VBM, reported in Figure 8, shows the contribution from both O and C atoms. In addition, similar to N<sub>2</sub> intercalation, the tilt angle between two octahedra approaches toward 180°, leading to a better overlap of W 5d and O 2p orbitals at the bottom of the CB, which shifts downward by ~0.02 eV. The shifts of the VBM and CBM lead to a band gap reduction of ~0.2 eV at the LDA level; the computed band gap of CO intercalated monoclinic WO<sub>3</sub> (1.13 eV) is direct at the  $\Gamma$  point. We note that the observed VBM upward shift is favorable for water splitting reactions, as the band alignment between monoclinic WO<sub>3</sub> and the H<sub>2</sub>O redox potential<sup>58</sup> is improved.

As in the case of  $N_2$ , we computed the energy change for incorporation of CO into WO<sub>3</sub>, and using nudge elastic band calculations, the kinetic barrier for CO to diffuse from a hollow center of the WO<sub>3</sub> crystal to a neighboring hollow center; the energy change is +1.2 eV, and the kinetic barrier is 2.9 eV, respectively, indicating that CO·8WO<sub>3</sub> is kinetically stable, as  $N_{2}$ , but not thermodynamically stable.

Rare Gases Intercalated WO<sub>3</sub>. We now turn to the discussion of rare gas intercalation in WO<sub>3</sub>. For rare gas atoms (e.g., Xe), we found the kinetic barrier for diffusing from a hollow center of the WO<sub>3</sub> crystal to a neighboring hollow center of the order of 2.5 eV in our nudged elastic band<sup>57</sup>

calculations, indicating that these atoms may be kinetically trapped in the oxide crystal. The formation energy of Xe intercalated WO<sub>3</sub> is +3.3 eV, rather high compared with the thermal energy at room temperature. However, the formation energy per WO<sub>3</sub> unit, 0.4 eV, is similar to that reported for dinitrogen in La–Ti systems,  $^{29}$  19–26 kJ mol<sup>-1</sup> LaTiO<sub>3.5</sub> (0.2–0.3 eV per LaTiO<sub>3.5</sub> unit).

Table 4 shows that the computed band gap  $(E_g)$  of WO<sub>3</sub> monotonically decreases with increasing size of the intercalated

Table 4. Band Gap  $(E_g)$  of Monoclinic WO<sub>3</sub> with Different Rare Gas Intercalation at 1:8 Ratio<sup>a</sup>

	atomic orbital energy	$E_{\mathrm{g}}$	$E_{ m g}'$	$\Delta$ -sol $E_{ m g}$	$\Delta E$
pure WO <sub>3</sub>	-9.20 [O 2p]	1.3		2.39	
+Ne	-13.54 [Ne 2p]	1.17	1.17	2.29	0.140
+Ar	-10.40 [Ar 3p]	1.19	1.19	2.26	1.248
+Kr	-9.39 [Kr 4p]	1.12	1.09	2.17	2.136
+Xe	-8.39 [Xe 5p]	0.38	1.13	1.85	3.304

"Also listed are the energies of oxygen and rare gas atom p orbitals evaluated  $^{30}$  by all-electron LDA calculations. The third column  $(E_{\rm g}')$  gives the band gap of the pure WO $_3$  crystals with geometries fixed to those of the corresponding optimized intercalated structures. The difference between indirect and direct band gaps is within 0.01 eV. In the fourth column we report the band gap  $(\Delta$ -sol  $E_{\rm g})$  obtained by the method of ref 39. In the fifth column we report the formation energy denoted by  $\Delta E$  defined as in Table 1. All energies are in eV.

rare gas atoms. For Ne, Ar, and Kr, we observed a moderate reduction by about 0.1-0.2 eV, while in the case of Xe the gap substantially decreases, by about 0.9 eV. If the intercalated atoms are removed while keeping the WO<sub>3</sub> geometry fixed, the band gaps  $(E_g')$  are reduced by 0.1-0.2 eV for all the rare gas atoms. The same trend as found with LDA calculations was also observed using the modified  $\Delta$ SCF method. This behavior can be explained by analyzing the 2-fold effect of rare gas intercalation: induced structural modifications, i.e., lattice expansion and distortion of the WO<sub>3</sub> lattice, and orbital hybridization and weak charge overlap between rare gas atoms and WO<sub>3</sub>. These effects are discussed below.

Similar to  $N_2$  intercalation, the tilt angle between octahedra increases rapidly toward 180° for Ne, Ar, and Kr intercalation: as expected, the bigger the atomic radius of the rare gas atoms, the larger the distortion induced in the lattice. The volume of intercalated WO3 increases by 2.5% (8WO3:Ne) to 7.2% (8WO3:Xe) compared to that of pure WO3. The expanded volume observed upon intercalation mainly comes from the increased tilt angle between octahedra ( $\angle$ W-O-W). When  $\theta_t$  increases from 160° to 180°, the bottom of the CB ( $t_{2g}$ ) is shifted downward, for the same reasons as those discussed in the case of  $N_2$ . (The relative position of the CB of the pure and intercalated solids has been obtained by aligning the W 5s core states. The 5s energy levels of W lie 70 eV below the VBM and are unaffected by the presence of intercalated atoms.)

While Ne and Ar weakly affect the band gap of the oxide, and Kr leads to a  $\sim$ 0.2 eV decrease, Xe-intercalated monoclinic WO<sub>3</sub> has a significant band gap reduction of 0.9 eV at the LDA level (see Table 4). This indicates the presence of a stronger interaction between Xe and the WO<sub>3</sub> lattice. This interaction arises thanks to the position of the 5p atomic orbitals of Xe, 0.8 eV higher in energy than the O 2p atomic orbitals. As previously discussed, the VBM of pure WO<sub>3</sub> is formed by the nonbonding O 2p states; therefore, the hybridization between

Xe 5p and O 2p states shifts upward the valence band edge and gives rise to midgap states (see Figure 10) whose presence

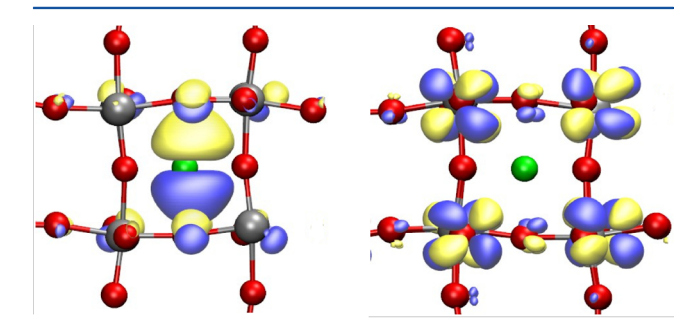


**Figure 9.** Isosurfaces of orbitals at the VBM (left panel) and CBM (right panel) of Xe-intercalated monoclinic WO<sub>3</sub> (green, Xe; red, O; silver, W). Yellow/blue spheres indicate (-)/(+) signs of the wave function phases.

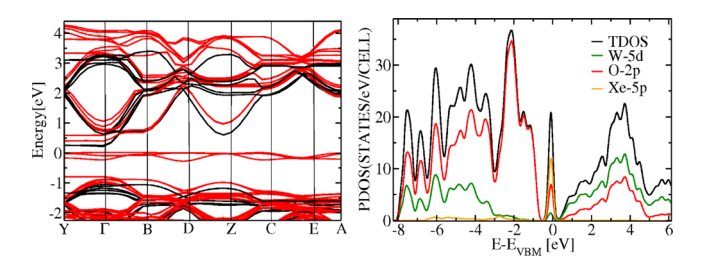


**Figure 10.** Left panel: Band structure of Xe-intercalated monoclinic WO<sub>3</sub> (red) as obtained with DFT-LDA calculations. For comparison, the band structure of pure monoclinic WO<sub>3</sub> obtained at the same level of theory is also shown (black). The two band structures are aligned at the energy of the W 5s core states. Right panel: Projected density of states (PDOS) and total density of states (TDOS) of Xe-intercalated monoclinic WO<sub>3</sub> as obtained within DFT/LDA; the zero of energy has been chosen at the VBM ( $E_{\rm VBM}$ ).

reduces the band gap. Note that, as in the case of CO intercalated WO $_3$ , the upward shift of the VB edge is a desirable feature, improving the band alignment with  $H_2O$  redox potential.

As shown in Figure 9, the VBM of Xe-intercalated WO<sub>3</sub> is mainly composed of O 2p nonbonding orbitals (perpendicular to the W–O bond) as in the case of pure WO<sub>3</sub>; at the same time, the wave function is partially residing on the Xe p orbital. The CBM remains dominated by W 5d  $t_{2g}$  and O 2p as in the absence of Xe. We note that, as in the case of N<sub>2</sub>, Xe is unexpectedly not inert in the oxide matrix.

Finally we investigated the band gap dependence on the exchange-correlation functional, by replacing the LDA functional with the hybrid PBE0 functional at the LDA optimized geometry, and found a band gap of 2.0 eV for Xe-intercalated WO $_3$ . The gap of pure WO $_3$  computed at the PBE0 level of theory is 3.28 eV, which, as noted earlier, is overestimated compared to the experimental value of 2.6 eV. Therefore, PBE0 calculations most likely provide an upper bound for the band gap of Xe-intercalated monoclinic WO $_3$ . One may expect the actual Xe intercalated band gap to be less than 2.0 eV (presumably of the order of 1.8 eV, as predicted at the  $\Delta$ SCF level of theory) which would be ideal for water oxidation applications.

Effects similar to those observed for Xe, though weaker, were found in the case of Kr. In the case of Ne and Ar, no orbital coupling between the Ne 2p (Ar 3p) and the O 2p states occurs

at the VB edge: the energy of the Ne 2p (Ar 3p) is 4 (1) eV lower than that of O 2p. The band structure (not shown) of Ne-intercalated monoclinic  $WO_3$  is similar to that of pure  $WO_3$  except that the CB shifts downward and the VB edge between Y (0, 0.5, 0) and B (0.5, 0,0) flattens out. Similar results are obtained also in the case of Ar. As a consequence for Ne and Ar intercalation the PDOS (not shown) is similar to that of pure  $WO_3$ : Ne and Ar p states are embedded deeply in the VB; the top of the VB is entirely composed of O p orbitals just as in pure  $WO_3$ .

#### SUMMARY AND CONCLUSIONS

We investigated the structural and electronic properties of clathrates of tungsten oxide containing nitrogen, and carbon monoxide molecules, and rare gas atoms. We found that intercalation of closed shell species in the oxide is a promising way to modify the host lattice electronic properties for water oxidation: no charge defects and thus no potential charge recombination centers are introduced, and the band gap of the oxide may be substantially decreased.

Stable clathrates with host N<sub>2</sub> molecules were recently synthesized, and our calculations provided an interpretation of the observed band gap reduction, as well as of the measured lattice expansion and Raman spectra. In addition, we predicted the properties of WO3 clathrates with CO and rare gas atoms inserted in the oxide lattice. We found that in all cases the band gap of intercalated WO<sub>3</sub> is reduced, due to the combined effect of structural and electronic changes occurring upon intercalation; however, the magnitude of the reduction and the relative shift of the conduction and valence band edges depend on the host molecule or atom. While in the case of N2 the position of the VBM is unaffected and the CBM moves downward, in the case of CO and Xe the VBM is moved upward, thus improving the alignment between the oxide VB and the water redox potential. However, in all clathrates of tungsten oxide investigated here, the hole mobility of the pure oxide is not improved by molecule or atom insertion, as shown by computed band structures, and improving hole mobilities remains an open issue.

For  $N_2$  concentrations close to those reported experimentally  $(xN_2\cdot WO_3, x=0.034-0.039)$ , we found a band gap reduction smaller than the measured one (0.2-0.35 eV), depending on the level of theory, instead of  $\sim 0.8 \text{ eV})$ . Interestingly, by optimizing the geometry and cell parameters with a nonlocal van der Waals density functional, we obtained the largest structural changes upon  $N_2$  insertion and the largest band gap reduction (0.35 eV). This indicates that the underestimate of band gap reduction with respect to experiment might be caused by an underestimate of the lattice distortions occurring upon insertion of  $N_2$  in the lattice. It is also possible that in the experimental samples, clustering of  $N_2$  occurs, and this would lead to a larger reduction of the band gap.

Work is in progress to study interfaces between liquid water and oxide clathrates, and to investigate the effect of surface defects and possible interface roughness on the electronic properties of the oxide.

#### ASSOCIATED CONTENT

#### **S** Supporting Information

Computational details, detailed analysis of structural properties and electronic structure of N<sub>2</sub>-intercalated simple cubic WO<sub>3</sub>, oxygen vacancy and nitrogen substitution in monoclinic WO<sub>3</sub>.

This material is available free of charge via the Internet at http://pubs.acs.org.

#### AUTHOR INFORMATION

# **Corresponding Author**

\*E-mail: yping@ucdavis.edu.

#### Notes

The authors declare no competing financial interest.

#### ACKNOWLEDGMENTS

This work was supported by Grant NSF-CHE-0802907. This work used the Extreme Science and Engineering Discovery Environment (XSEDE), which is supported by National Science Foundation Grant OCI-1053575. Calculations were also performed at the UC Shared Research Computing Service facilities at the University of California, Berkeley. Y.L. was partially supported by DOE Grant DE-AC02-98CH10886. The authors thank Qixi Mi, Bingfei Cao, Bruce S. Brunschwig, Peter Khalifah, Nathan Lewis, and Harry Gray for many useful discussions.

### **■** REFERENCES

- (1) Butler, M.; Nasby, R.; Quinn, R. K. Solid State Commun. 1976, 19, 1011–1014.
- (2) Miller, E. L.; Paluselli, D.; Marsen, B.; Rocheleau, R. E. Sol. Energy Mater. Sol. Cells 2005, 88, 131–144.
- (3) Miller, E. L.; Marsen, B.; Cole, B.; Lum, M. Electrochem. Solid-State Lett. 2006, 9, G248-G250.
- (4) Seabold, J. A.; Choi, K.-S. Chem. Mater. **2011**, 23, 1105–1112.
- (5) Zheng, H.; Tachibana, Y.; Kalantar-zadeh, K. Langmuir 2010, 26, 19148–19152.
- (6) Su, J.; Guo, L.; Bao, N.; Grimes, C. A. Nano Lett. 2011, 11, 1928–1933.
- (7) Park, H.; Kim, K. Y.; Choi, W. J. Phys. Chem. B 2002, 106, 4775–4781.
- (8) Hill, J. C.; Choi, K.-S. J. Phys. Chem. C 2012, 116, 7612-7620.
- (9) Huda, M. N.; Yan, Y.; Moon, C.-Y.; Wei, S.-H.; Al-Jassim, M. M. *Phys. Rev. B* **2008**, *77*, 195102.
- (10) Paluselli, D.; Marsen, B.; Miller, E. L.; Rocheleau, R. E. Electrochem. Solid-State Lett. 2005, 8, G301–G303.
- (11) Tang, J.; Ye, J. J. Mater. Chem. 2005, 15, 4246-4251.
- (12) Maruthamuthu, P.; Ashokkumar, M.; Gurunathan, K.; Subramanian, E.; Sastri, M. Int. J. Hydrogen Energy 1989, 14, 525–528.
- (13) Wang, F.; Di Valentin, C.; Pacchioni, G. J. Phys. Chem. C 2012, 116, 8901–8909.
- (14) Wang, F.; Di Valentin, C.; Pacchioni, G. Phys. Rev. B **2011**, 84, 073103.
- (15) Goodenough, J. B. Prog. Solid State Chem. 1971, 5, 145-399.
- (16) Hjelm, A.; Granqvist, C. G.; Wills, J. M. Phys. Rev. B 1996, 54, 2436–2445
- (17) Brown, B. W.; Banks, E. J. Am. Chem. Soc. 1954, 76, 963-966.
- (18) Stachiotti, M. G.; Cora, F.; Catlow, C. R. A.; Rodriguez, C. O. *Phys. Rev. B* **1997**, *55*, 7508–7514.
- (19) Asahi, R.; Morikawa, T.; Ohwaki, T.; Aoki, K.; Taga, Y. Science **2001**, 293, 269–271.
- (20) Wang, J.; Tafen, D. N.; Lewis, J. P.; Hong, Z.; Manivannan, A.; Zhi, M.; Li, M.; Wu, N. J. Am. Chem. Soc. 2009, 131, 12290–12297.
- (21) Livraghi, S.; Paganini, M. C.; Giamello, E.; Selloni, A.; Di Valentin, C.; Pacchioni, G. J. Am. Chem. Soc. **2006**, 128, 15666–15671.
- (22) Batzill, M.; Morales, E. H.; Diebold, U. Phys. Rev. Lett. 2006, 96, 026103.
- (23) Nakamura, R.; Tanaka, T.; Nakato, Y. J. Phys. Chem. B 2004, 108, 10617–10620.
- (24) Hoang, S.; Guo, S.; Hahn, N. T.; Bard, A. J.; Mullins, C. B. Nano Lett. 2012, 12, 26–32.

(25) Cole, B.; Marsen, B.; Miller, E.; Yan, Y.; To, B.; Jones, K.; Al-Jassim, M. *J. Phys. Chem. C* **2008**, *112*, 5213–5220.

- (26) Yin, W.-J.; Tang, H.; Wei, S.-H.; Al-Jassim, M. M.; Turner, J.; Yan, Y. *Phys. Rev. B* **2010**, 82, 045106.
- (27) Mi, Q.; Ping, Y.; Li, Y.; Cao, B.; Brunschwig, B. S.; Khalifah, P.; Galli, G. A.; Gray, H. B.; Lewis, N. S. *J. Am. Chem. Soc.* **2012**, DOI: 10.1021/ja3067622.
- (28) Gendre, L. L.; Marchand, R.; Laurent, Y. J. Eur. Ceram. Soc. 1997, 17, 1813-1818.
- (29) Tessier, F.; Le Gendre, L.; Chevire, F.; Marchand, R.; Navrotsky, A. Chem. Mater. 2005, 17, 3570-3574.
- (30) Giannozzi, P.; et al. J. Phys. Condens. Matter 2009, 21, 395502.
- (31) http://eslab.ucdavis.edu/software/qbox.
- (32) Perdew, J. P.; Burke, K.; Ernzerhof, M. Phys. Rev. Lett. 1996, 77, 3865-3868.
- (33) Perdew, J. P.; Ernzerhof, M.; Burke, K. J. Chem. Phys. 1996, 105, 9982–9985.
- (34) Dion, M.; Rydberg, H.; Schröder, E.; Langreth, D. C.; Lundqvist, B. I. *Phys. Rev. Lett.* **2004**, *92*, 246401.
- (3S) Thonhauser, T.; Cooper, V. R.; Li, S.; Puzder, A.; Hyldgaard, P.; Langreth, D. C. *Phys. Rev. B* **2007**, *76*, 125112.
- (36) Román-Pérez, G.; Soler, J. M. Phys. Rev. Lett. 2009, 103, 096102.
- (37) Lee, K.; Murray, E. D.; Kong, L.; Lundqvist, B. I.; Langreth, D. C. *Phys. Rev. B* **2010**, *82*, 081101.
- (38) Murray, E. D.; Galli, G. Phys. Rev. Lett. 2012, 108, 105502.
- (39) Chan, M. K. Y.; Ceder, G. Phys. Rev. Lett. 2010, 105, 196403.
- (40) Wijs, G. A. d.; Boer, P. K. d.; Groot, R. A. d.; Kresse, G. *Phys. Rev. B* **1999**, *59*, 2684–2693.
- (41) Cora, F.; Stachiotti, M. G.; Catlow, C. R. A.; Rodriguez, C. O. J. Phys. Chem. B 1997, 101, 3945–3952.
- (42) Chatten, R.; Chadwick, A. V.; Rougier, A.; Lindan, P. J. D. J. Phys. Chem. B **2005**, 109, 3146–3156.
- (43) Wang, F.; Di Valentin, C.; Pacchioni, G. J. Phys. Chem. C 2011, 115, 8345–8353.
- (44) The difference between our results and those of ref 43 may be due to the use of different basis sets (Gaussian basis sets in ref 43 and plane waves in the present work) and different geometries (optimized at the LDA level here, but at the PBE0 level in ref 43).
- (45) Bullett, D. W. J. Phys. B: Solid State 1983, 16, 2197.
- (46) Loopstra, B. O.; Rietveld, H. M. Acta Crystallogr., Sect. B 1969, 25, 1420-1421.
- (47) Kehl, W. L.; Hay, R. G.; Wahl, D. J. Appl. Phys. 1952, 23, 212-215.
- (48) Ackermann, R. J.; Sorrell, C. A. J. Appl. Crystallogr. 1974, 7, 461–467.
- (49) Iwai, T. J. Phys. Soc. Jpn. 1960, 15, 1596-1600.
- (50) In the band structure of a  $(2 \times 2 \times 2)$  simple cubic unit cell, the high symmetry points Y, B, Z are equivalent, while they are slightly inequivalent in the monoclinic phase (see Figure 2b).
- (51) Henkelman, G.; Uberuaga, B. P.; Jonsson, H. J. Chem. Phys. **2000**, 113, 9901–9904.
- (52) Li, Y.; Galli, G. Appl. Phys. Lett. 2012, 100, 071605.
- (53) Fang, C.; de Wijs, G.; Orhan, E.; de With, G.; de Groot, R.; Hintzen, H.; Marchand, R. J. Phys. Chem. Solids 2003, 64, 281–286.
- (54) We obtained the same results for  $\Delta \rho$  at the LDA and PBE0 level of theory.
- (55) The Y(0,0.5,0) point corresponds to the (0,0,0.5) point in refs 42 and 9, because the y and z coordinates are switched in our calculations with respect to those adopted in ref 42.
- (56) Hartwigsen, C.; Goedecker, S.; Hutter, J. *Phys. Rev. B* **1998**, 58, 3641–3662.
- (57) Henkelman, G.; Uberuaga, B. P.; Jonsson, H. J. Chem. Phys. 2000, 113, 9901–9904.
- (58) Weinhardt, L.; Blum, M.; Bar, M.; Heske, C.; Cole, B.; Marsen, B.; Miller, E. L. *J. Phys. Chem. B* **2008**, *112*, 3078–3082.